The Role of Cr, P, and N Solutes on the Irradiated Microstructure of bcc Fe

Patrick H. Warren[1*], Caleb Clement[1], Chao Yang[1], Amrita Sen[1], Wei-Ying Cheng[2], Yaqiao Wu[3,4], Ling Wang[5], Janelle P. Wharry[1]

1 School of Materials Engineering, Purdue University, West Lafayette, IN 47906, USA

2 Argonne National Laboratory, Lemont, IL 60439, USA

3 Micron School of Materials Science & Engineering, Boise State University, Boise, ID 83725, USA

4 Center for Advanced Energy Studies, Idaho Falls, ID 83401, USA

5 High Energy Density Science Division, SLAC National Accelerator Laboratory, Menlo Park, CA 94025, USA

* Corresponding Author:

Patrick H. Warren

2720 Doris Circle, Idaho Falls, ID, 83402

(208) 709-0915

warrenp@purdue.edu

Abstract

The objective of this study is to understand irradiation-induced and assisted defect evolution in binary body center cubic (bcc) Fe-based alloys. The broader class of bcc ferritic alloys are leading candidates for advanced nuclear fission and fusion applications, in part due to their exceptional void swelling resistance. However, their irradiated microstructure evolution is sensitive to solute species present, since these solutes can act as traps for irradiation-induced defects due to the surrounding tensile or compressive stress fields. Here, three alloys (Fe-9.5%Cr, Fe-4.5%P, and Fe-2.3%N) are selected for study because they systematically exhibit varying solute sizes and solute positions (i.e., substitutional or interstitial). *Ex situ* and *in situ* ion irradiations reveal that Fe-P has a considerably finer and denser population of irradiation-induced defects than Fe-Cr and Fe-N at the same irradiation conditions, which is attributed to strong defect trapping at undersized substitutional P, consequently hindering the development of extended defects. Meanwhile, oversized substitutional solutes (e.g., Cr) and interstitial solutes (e.g., N) may also suppress dislocation loop development due to weak solute-defect trapping.

1. Introduction

Ferritic alloys have been the subject of extensive investigation for next generation nuclear fission and fusion reactor applications, because of their exceptional high temperature strength and their extreme swelling resistance compared to austenitic stainless steels [1]. However, the shift of the ductile to brittle transition temperature to higher temperatures as a result of irradiation embrittlement is problematic, and researchers have investigated tailoring the alloying species and their compositions to improve ductility [2,3]. But at the same time, it is well known that alloying additions can also alter the irradiation-induced microstructure evolution [4] since solutes act as traps for irradiation defects due to the tensile or compressive stress fields around them.

Amongst the most thoroughly studied alloying additions in ferritic steels is Cr because of its contribution to improved corrosion resistance, high temperature oxidation resistance, and low activation. However, irradiation embrittlement occurs especially at low temperatures, resulting from radiation-induced microstructural changes including dislocation loop evolution and the formation of Cr-rich α' phases [5–11]. Many of these irradiation effects on microstructure are at least partially influenced by the substitutional nature of Cr.

Substitutionality can also occur for impurity elements such as P in ferrite. The addition of P has produced mixed results in ferritic steels. Some studies have shown the presence of P can limit the growth of precipitates such as MC type carbides and improve the rupture lifetime [12–15]. Other studies have shown P can limit the growth of radiation induced defects and slow the progression of radiation damage [16].

Interstitial solutes such as N are also typically considered an impurity element in structural alloys. However, the addition of N has been expressly investigated because of its key role in mechanical behavior, particularly under irradiation. For example, N is associated with reduction in irradiation-induced localized deformation [17] as well as a reduction in the ductile to brittle transition temperature [2]. Studies have also demonstrated reduced irradiation hardening with the addition of N [18,19]. However, the role of N on irradiated microstructure evolution is poorly understood with often contradictory observations. That is, while some studies have shown that N reduces void and dislocation loop density [20], other studies have found N to increase dislocation loop density as a result of reduced self-interstitial atom (SIA) mobility [21,22].

There remain gaps in our understanding of exactly how various solute additions influence the accumulation of irradiation damage. In this work, we will systematically investigate the role of substitutional (both oversized and undersized) and interstitial species on the irradiated microstructure of bcc ferrite. Model binary Fe-Cr, Fe-P, and Fe-N alloys are irradiated using both *ex situ* and *in situ* techniques. Subsequently, transmission electron microscopy (TEM) imaging and chemical analyses are conducted to evaluate the irradiated microstructures. Irradiation induced or assisted defect densities – including loops, loop nuclei, and clusters – are quantified across the three alloys, and are explained in the context of trapping strength. Combining the present results with data from other binary alloys in the archival literature enables us to draw some generalized trends for irradiated microstructures containing classes of solutes (e.g., oversized substitutional, undersized substitutional, interstitial).

2. Methods

2.1 Bulk ex situ Irradiation & Characterization

Arc melted buttons of three Fe-*X* (where *X* = P, Cr, N) binary alloys were prepared by Ames Laboratory Materials Preparation Center: Fe-4.5%P, Fe-9.5%Cr, and Fe-2.3%N (all in at%). Both the Fe-Cr and Fe-N specimen contained a single α phase, while the Fe-P specimen contained a three-phase microstructure of an α-Fe-P matrix with intergranular Fe_3P precipitates, and P depleted α Fe "islands" contained within the Fe_3P precipitates. For the remainder of this document the relatively high α Fe-P region will be referred to as the Fe-P region because of the relatively high P content in that region while the P depleted α Fe island will simply be referred to as the α Fe region. The alloy buttons were then cut into 2 mm x 2 mm x 20 mm bars by electrical discharge machining. Two sets of bars were then mechanically polished, one set to be used as the non-irradiated reference set and the other to be irradiated. Mechanical polishing was carried out using Si carbide paper up through 1200 grit, then polished on a pad with 6 μm and 3 μm diamond slurries. Finally, samples were vibratory polished with a 0.5 μm silica slurry.

One set of polished samples was irradiated in the Wolverine 3 MV tandem particle accelerator at the Michigan Ion Beam Laboratory with 4.4 MeV Fe^{2+} ions at a temperature of 370 ± 5°C. Note the irradiation temperature was below phase transformation temperatures for all three alloys based on their phase diagrams, Figures S1-S3 in the supplementary information [23]. The irradiation damage profile was determined using Stopping Range of Ions in Matter (SRIM) in the quick Kinchin-Pease damage calculation mode; Figure 1(a). provides the dose as a

function of depth profile for the Fe-*X* alloys. The gray shaded region in Figure 1(a) indicates the 400-600 nm depth range analyzed, which had a dose of 8.5 displacements per atom (dpa) with a stage current of 0.833 μA, at a dose rate of 7.6×10^{-4} dpa/sec. This analysis depth was selected because both the surface sink effect and Fe implantation peak were avoided [24].

Transmission electron microscopy (TEM) lamellae of thicknesses ranging 45-80 nm were created and extracted from the reference and irradiated samples using a Quanta 3D FEG dual-beam scanning electron microscope (SEM)/focused ion beam (FIB) with Omniprobe micromanipulator. Thicknesses of the TEM lamellae were determined by SEM measurement after thinning and EELS thickness measurement. The SEM/FIB was operated at an accelerating voltage of 30 kV and beam current ranging from 7 nA to 1 nA for the milling of trenches and finer cleaning, respectively. Extracted lamellae were welded to a Cu half-grid by Pt deposition, then thinned to less than 100 nm using an acceleration voltage of 30 kV and beam currents ranging from 1 nA at the initial thinning stages, down to 49 pA at the final thinning stages. A final cleaning step with accelerating voltages of 5 kV and 2 kV and beam currents of 48 pA and 27 pA was used to reduce FIB damage from the surface of the lamella.

TEM imaging of the irradiated microstructure was done using bright field scanning TEM (BFSTEM) on a FEI Tecnai TF30-FEG STwin TEM at the Microscopy and Characterization Suite (MaCS) at the Center for Advanced Energy Studies (CAES). TEM diffraction analysis was used to determine the crystal structures and orientations. Dislocation loops and other irradiation-induced defects were imaged using down-zone axis BFSTEM, which has been demonstrated as an effective loop imaging approach, especially for bcc/ body center tetragonal (bct) steels [25]. As compared to conventional loop imaging techniques such as rel-rod imaging, down-zone axis

BFSTEM offers the distinct advantage of enabling observation of all loop types simultaneously (i.e., free of extinction conditions), allowing for more accurate defect density quantification. Ex situ irradiation induced and assisted defect densities, which included dislocation loops and clusters, were determined by averaging the defect counts of four separate micrographs from each of the Fe-X binary alloys. The major diameters of at least one hundred loops from were measured to determine the average dislocation loop diameters. STEM electron dispersive spectroscopy (EDS) with a dwell time of five minutes per pixel was used to produce elemental maps over areas of 0.056 μm^2 using a Thermo Scientific Themis Z at the Birck Nanotechnology Center at Purdue University. EDS maps have been cropped down to an area of 0.017 μm^2 in Figure 5. TEM selected area electron diffraction (SAED) patterns were used to determine the orientations of the samples.

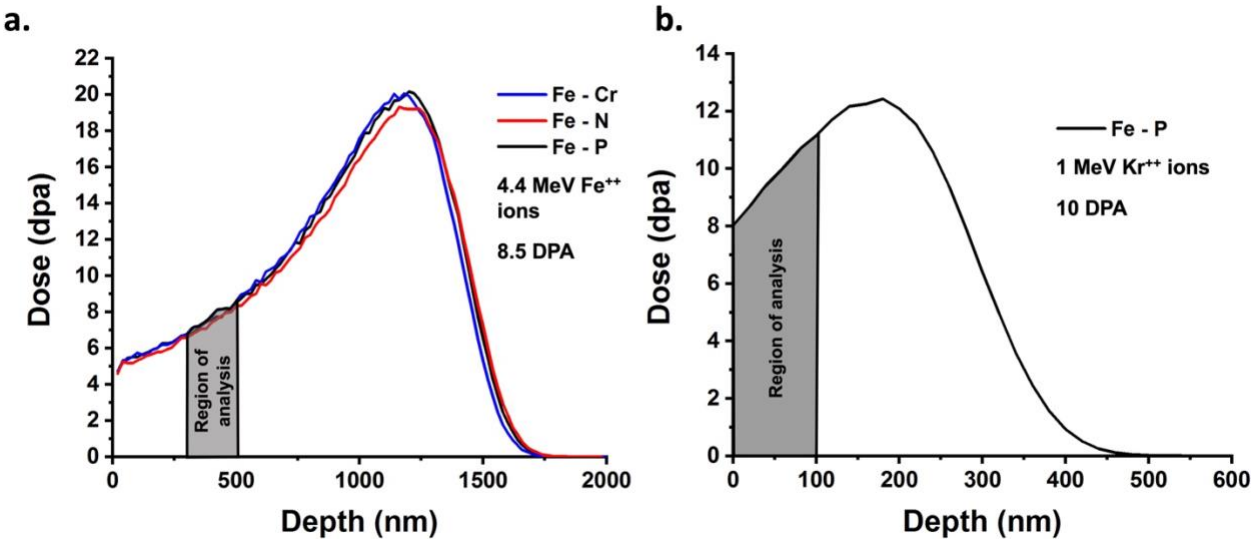

Figure 1 *: SRIM irradiation damage (dpa) profiles with regions of interest for microstructure characterization indicated in gray for (a) Fe-Cr, Fe-N, and Fe-P irradiated with 4.4 MeV Fe^{2+} ions; and (b) Fe-P irradiated with 1 MeV Kr^{2}+ ions.*

2.2 In situ Irradiation & Characterization

An additional TEM lamella from the reference Fe-P bar was milled by FIB following the method described in Section 2.1. The lamella was irradiated at the Intermediate Voltage Electron Microscope (IVEM)-Tandem facility at Argonne National Laboratory with 1 MeV Kr^{2+} ions at 370 °C up to a dose of 10 dpa. The ion energy of 1 MeV was chosen to ensure ion penetration through the thickness of the lamella, and also to reduce the irradiation fluence gradient throughout the thickness of the of the lamella, Figure 1(b). The irradiation temperature was chosen for consistency with the bulk *ex situ* Fe^{2+} ion irradiation. Prior to beginning *in situ* irradiation, the sample was annealed *in situ* within the TEM at 400°C and at 430°C for ten minutes at each temperature to further reduce FIB induced damage and to allow for better visibility of radiation induced or assisted microstructural evolution. The annealing temperature was raised from 400 ° C to 430 ° C to increase the rate of defect removal.

The as-fabricated Fe-P contained a three-phase structure of α-ferrite Fe-P matrix, β-Fe_3P precipitates, and α-Fe "islands" located within the β-phases, as shown in Figure 2 (a), pre annealed and (b) annealed at 400 °C and (c) annealed at 400 °C. Figure 2 (a) highlights the regions that were imaged during the irradiation, the matrix region outside of the β precipitate and an α Fe phase inside of the β precipitate. It should be noted that the α Fe phase enclosed in the β precipitate is not pure Fe but will be referred to as the α Fe region for the remainder of this study because of the depleted P in this region as seen in the EDS maps from Figure 7. The yellow dotted circle in Figure 2 (d) highlights a phase that began to form during the 430 °C annealing step which was not seen before annealing or at the 400 °C annealing step which

indicates that thermally activated phase change was not triggered until the temperature reached 430 °C. Tracking both the α-ferrite Fe-P and pure α-Fe regions during TEM *in situ* irradiation enabled us to understand the role of P on microstructure evolution. Specifically, TEM resolution video was recorded throughout the duration of the *in situ* irradiation at a fixed location in the α-ferrite matrix. The irradiation was paused at 0.5 dpa, 1 dpa, 3 dpa, 6 dpa, and 10 dpa to collect TEM images from within an α island. The tracked regions are identified by yellow dotted boxes in Figure 2**.** Throughout irradiation, bright field TEM imaging was used to characterize dislocation loops and precipitates, including P-rich clusters.

The post-irradiation lamella was examined using the Thermo Fisher Scientific Talos F200X S/TEM at the Irradiated Materials Characterization Laboratory (IMCL) at the Idaho National Laboratory (INL). Scanning TEM (STEM) energy dispersive x-ray spectroscopy (EDS) compositional analysis was conducted in the Fe-P region at a magnification of 453.7 kx with a 20 μs dwell time and a pixel size of 215 x 215 pm. STEM EDS in the α-Fe region was conducted at a magnification of 323.3 kx with a 20μs dwell time and a pixel size of 302 x 302 pm.

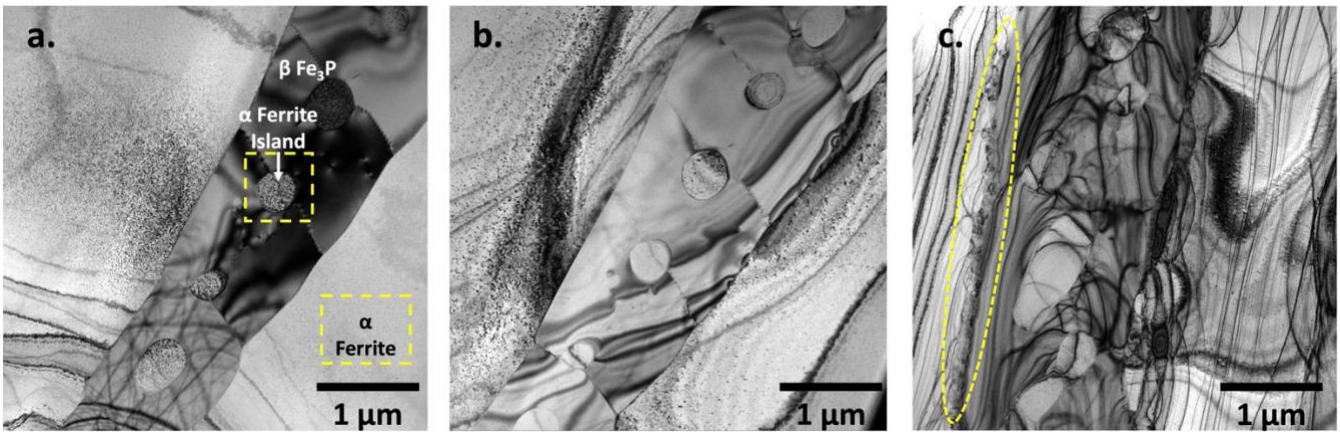

***Figure 2**: (a) Phases in Fe-P lamella, with specific regions of interest tracked during TEM in situ irradiation marked by yellow boxes before annealing (b) after 400 ℃ anneal(c) separate B precipitate of same sample with yellow dotted circle indicating new phase formation after 430 ℃ anneal.*

3. Results

3.1 Nature of Solute Atoms

TEM SAED patterns inform the lattice parameters of the three alloys by measurement of the *d*-spacings, insets in Figure 3. The relationship between *d*-spacing and lattice parameter is highlighted in Equation S1 in the supplementary information [26]. The lattice parameters measured for Fe-Cr, Fe-N, and Fe-P are 0.295 Å, 0.295 Å, and 0.291 Å, respectively. Oversized substitutional solutes and all interstitial solutes are expected to produce a lattice expansion, while undersized substitutional solutes are expected to result in a lattice contraction. Numerous studies have established that Cr is an oversized substitutional atom, P is an undersized substitutional atom, and N is an interstitial atom in α-Fe [27–31]. The relative lattice parameters measured here corroborate that the solute species are taking their expected substitutional or interstitial positions within the alloys studied. SEM Electron backscatter diffraction (EBSD) maps of the Fe-Cr, Fe-N, and Fe-P alloys (Figure S4 and S5 in the

supplementary information) show no evidence of multiple phases. There are clusters of randomly oriented pixels in the EBSD map of the Fe-N alloy in Figure S5 (c) of the supplementary information. It should be noted that those are from FIB fiduciary marks that were made in this sample to locate specific regions of the sample. However, the intergranular Fe_3P β-phases, indicated by black dotted borders in Figure S4, are visible in the Fe-P EBSD map. The grains of the Fe-P and Fe-N samples are tens to several hundred μm in size while the grains in the Fe-Cr sample are tens of μm in size and in some cases less than ten μm. BFSTEM micrographs of the as received Fe-Cr, Fe-P, and Fe-N samples have also been included in the supplementary information in Figure S6 (a-c).

3.2 Ex Situ Irradiated Microstructures

Comparative irradiated microstructure characterization across the three alloys focuses on dislocation loop and cluster/precipitate type defects, all of which tend to be difficult to distinguish from one another especially in low fluence, high flux ion irradiation conditions [32]. The Fe-Cr irradiated microstructure, shown in Figure 3(a), exhibits a mixture of dislocation loops, clusters, and dislocation line segments. However, only the three-dimensional defects (i.e., loops and clusters) are in included in the quantification of irradiation defects. Hence, the number density of defects in Fe-Cr is 1.59×10^{22} m^{-3}. The Fe-N irradiated microstructure is similarly comprised of dislocation lines, dislocation loops, and clusters, Figure 3(b), but with a lower total defect (i.e., loops and clusters) density of 9.85×10^{21} m^{-3}. The irradiated Fe-P microstructure, on the other hand, is comprised of a fine and highly dense dispersion of apparent nanoscale clusters or loop nuclei, Figure 3(c), at a significantly higher number density

of 6.02 x 10^{22} m^{-3}. These differences in defect densities and defect morphologies across the alloys can be clearly discerned from the down-zone TEM micrographs in Figure 3, and are quantitatively compared in Figure 4(a).

The diffraction pattern insets in Figure 3 provide further insight into the nature of the defects. Specifically, the Fe-P diffraction pattern has distinct and strong diffraction spots representing the α-ferrite matrix, as well as faint rings suggesting a secondary phase. Higher magnification TEM imaging of the same region in the irradiated Fe-P sample reveals isolated Moiré fringes, enclosed by red dotted circles in Figure 3(d), which corroborate the presence of a coherent precipitate phase [26,33]. These precipitates range 5 – 8 nm in size at a density of 2.25 x 10^{21} m^{-3}, determined by measuring and counting the Moiré fringe defects in Figure 3(d); these precipitates represent a relatively small portion of the total defects in the Fe-P specimen. Diffraction patterns from the Fe-Cr and Fe-N specimens do not show any indications of precipitation.

Quantitatively, defect sizes appear inversely related to number densities, Figure 4(a). The Fe-Cr average defect diameter is 6.7 ± 3.1 nm, whereas the Fe-N which has lower defect density has a larger average defect diameter of 7.8 ± 3.3 nm. By contrast, the Fe-P has highest defect density but the smallest average defect diameter at 5.3 ± 1.5 nm. Defect size distributions are compared in Figure 4(b). The Fe-P defect size distribution has a notably lower standard deviation and skewness than the Fe-Cr and Fe-N defect size distributions, further suggesting that the defect types in Fe-P differ from those in Fe-Cr and Fe-N.

STEM EDS maps reveal chemical clustering of P in the irradiated Fe-P specimen, coincident with dark-contrast defects seen in TEM, Figure 5. On the other hand, no chemical

clustering or segregation is observed in the irradiated Fe-Cr and Fe-N, Figure 5. The EDS map of the Fe-P alloy was collected at a lower magnification than the other two alloys. As such the full image has been cropped to show a representative region with P solute clusters visible. The full EDS map image of the Fe-P sample is provided in Figure 5 in the supplementary information in Figure S7. This finding is further confirmation of the precipitate-like nature of the irradiation induced or assisted defects in Fe-P, while the defects in Fe-Cr and Fe-N are more likely loops or loop nuclei. It should be noted that the clusters identified in the BFSTEM images in Figure (a-d) are point defect clusters while the clusters identified in the EDS maps in Figure 5 (a-i) are solute clusters.

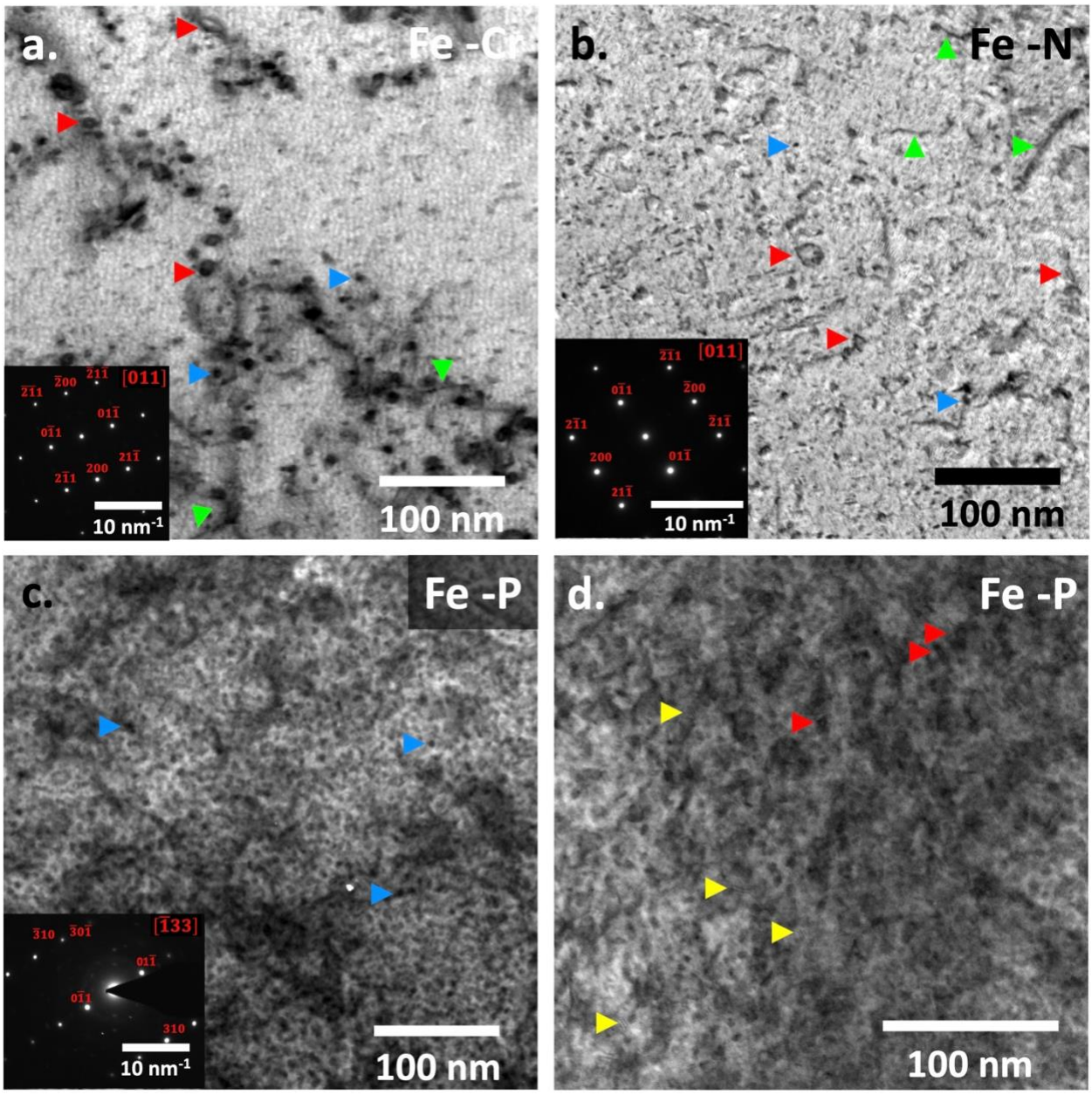

Figure 3*: TEM micrographs with inset diffraction patterns of ex situ irradiated (a) Fe-Cr, (b) Fe-N, and (c) Fe-P, with (d) showing higher resolution image of defect in Fe-P revealing Moiré fringes indicative of precipitation. Dislocation loops, dislocation lines, clusters, and precipitates are indicated by red, green, blue, and yellow arrows respectively.*

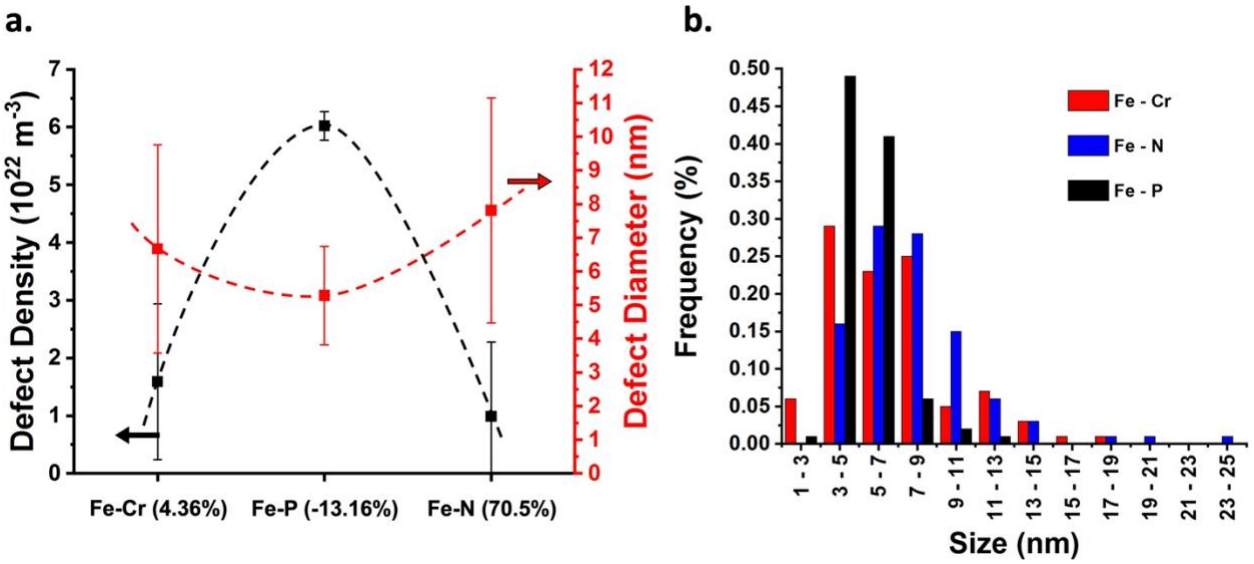

***Figure 4**: Comparison of (a) defect number densities and average defect diameter as a function of size factor magnitude (note that although the data are plotted in order of size factor magnitude, the true size factor values are given, with negative values indicating undersized solutes); and (b) defect size distributions across the alloys following ex situ irradiation.*

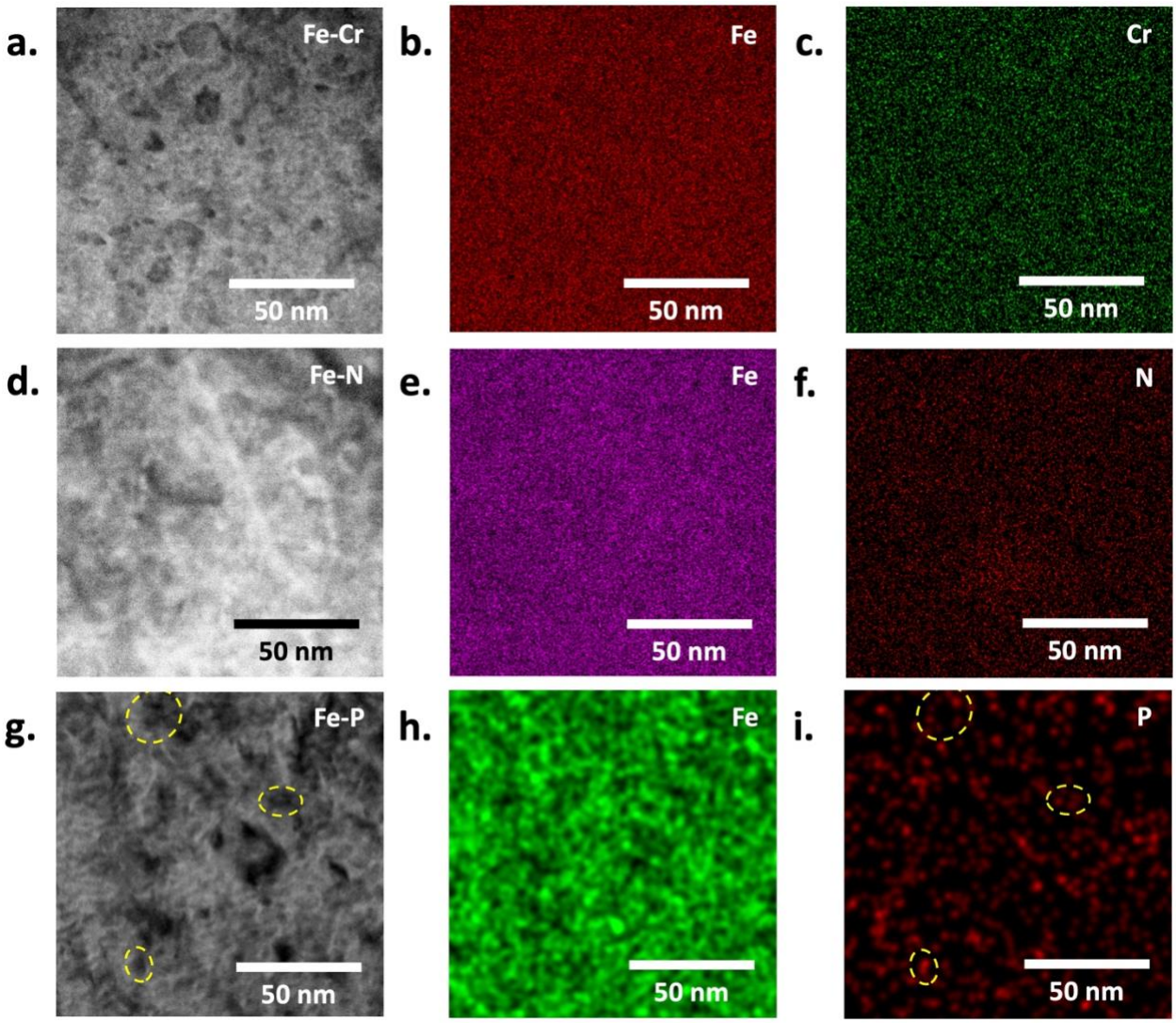

Figure 5*: Reference images and STEM EDS maps of irradiated (a-c) Fe-Cr, (d-f) Fe-N, and (g-i) Fe-P. Yellow dotted circles in Fe-P reference image (g) and P EDS map (i) show defect clusters and loops that exhibit P segregation.*

3.2 In situ TEM Irradiation of α-Fe and Fe-P

The *in situ* irradiation-induced defect evolution of the α-Fe and Fe-P regions are notably different, with the α-Fe exhibiting classic dislocation loop nucleation and growth, while the Fe-P generates defects similar to those observed by *ex situ* irradiation. These distinct behaviors are

illustrated in a series of bright field TEM micrographs taken during *in situ* irradiation at doses of 1, 3, 6, and 10 dpa, shown in Figures 6-9. Figures 6-7 focus on the α-Fe region, while Figures 8-9 focus on the Fe-P region. For both phase regions, micrographs first present the loop and defect microstructure evolution (Figures 6 and 8), then subsequently present the precipitate evolution (Figures 7 and 9).

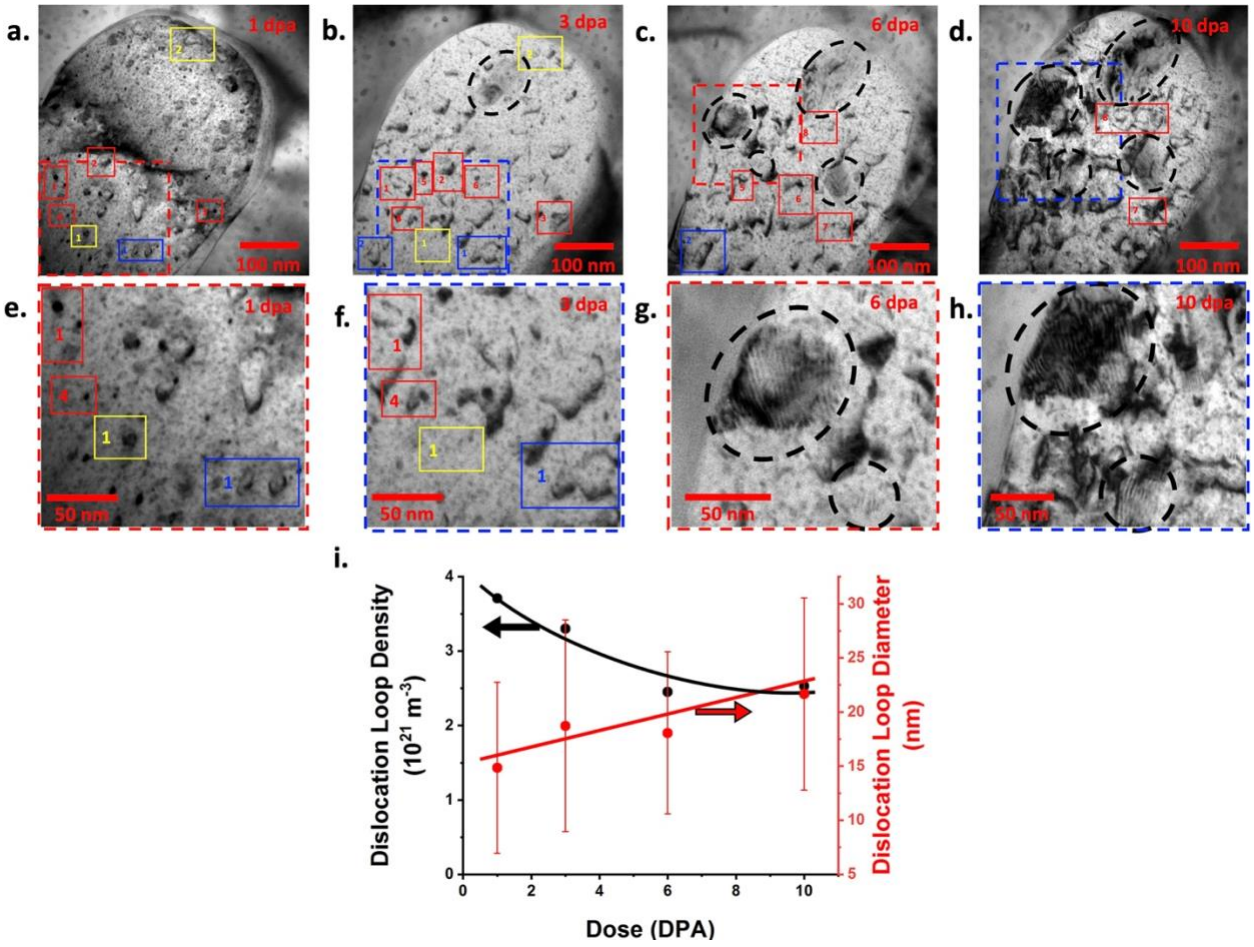

***Figure 6**: Defect and loop evolution in α-Fe during in situ irradiation, shown by TEM bright field micrographs at doses of (a) 1 dpa, (b) 3 dpa, (c) 6 dpa, and (d) 10 dpa; with red and blue dashed boxes shown at higher magnification in TEM bright field images at (e) 1 dpa, (f) 3 dpa, (g) 6 dpa, (h) 10 dpa. In (a)-(h), red, yellow, and blue boxes and black dashed circles indicate loops/loop nuclei growing, loops escaping to surface of sample, loops*

merging, and formation and growth of precipitates respectively. (i) Plot of dislocation loop diameter and number density as a function of dose.

In α-Fe, loop nuclei (which appear in TEM as "black dots") form at doses <1 dpa and rapidly grow into fully resolvable dislocation loops by 1 dpa. This nucleation-and-growth process occurs continuously throughout the duration of irradiation, with new loop nuclei appearing at all dose increments imaged. Examples of this loop nucleation-and-growth behavior are enclosed in numbered red boxes and can be tracked across all doses in Figure 6(a)-(d). Some loops can be seen merging to form into a single loop, examples of which are enclosed in numbered blue boxes. Additionally, some loops seem to disappear with increasing dose (yellow numbered boxes), indicating their removal at the surface sink, which is a known occurrence in TEM *in situ* irradiated lamellae [8,34–36]. These loop behaviors culminate in quantitative loop growth with increasing dose, from 14.8 ± 7.9 nm at 1 dpa, to 21.7 ± 8.9 nm at 10 dpa. Dislocation loop density decreases from 3.71 x 10^{21} m^{-3} at 1 dpa to 2.53 x 10^{21} m^{-3} at 10 dpa, representing typical loop growth and coarsening. It is also known that as loops grow in size, they become stronger sinks for point defects, which has the combined effect of limiting loop nucleation while contributing to loop growth [37]. These trends in dislocation loop density and average diameter are shown as a function of dose for the α-Fe region in Figure 6(i); note that these quantitative measurements exclude the loop nuclei that appear as "black dot" type defects, until they become resolvable as actual loops.

Radiation-assisted precipitation also occurs in the α-Fe, first appearing at 3-6 dpa and growing with increasing dose. These precipitates, typically ~10s of nm in size and enclosed by

the red dashed circle in Figure 6(b)-(d). The Moiré fringe spacing within the precipitates increases with dose, as shown for a selected precipitate in Figure 7(a)-(d). Post-irradiation STEM EDS chemical mapping, Figure 7(e)-(i), reveals these precipitates are Fe-rich carbides. The Fe_3C cementite phase is well known to precipitate in steels and has a larger lattice parameter than ferrite. These carbides are believed to have formed from C contamination from both the environment the TEM lamella was exposed to after it was made as well as C injection during ion irradiation, both of which are well known causes of C contamination [38–40]. Hence, the increasing Moiré fringe spacing suggests that lattice expansion may be occurring as the precipitates tend toward their steady-state composition and structure. Figure 7 (j-l) provide reference image and Fe, P, and C EDS maps of an unirradiated α Fe region. The unirradiated EBSD maps demonstrate that the phases seen in Figure 7 (a-h) are either induced are assisted by irradiation. Lower magnification reference image and Fe and P maps of the same unirradiated α Fe island and are provided in the supplemental information Figure S8.

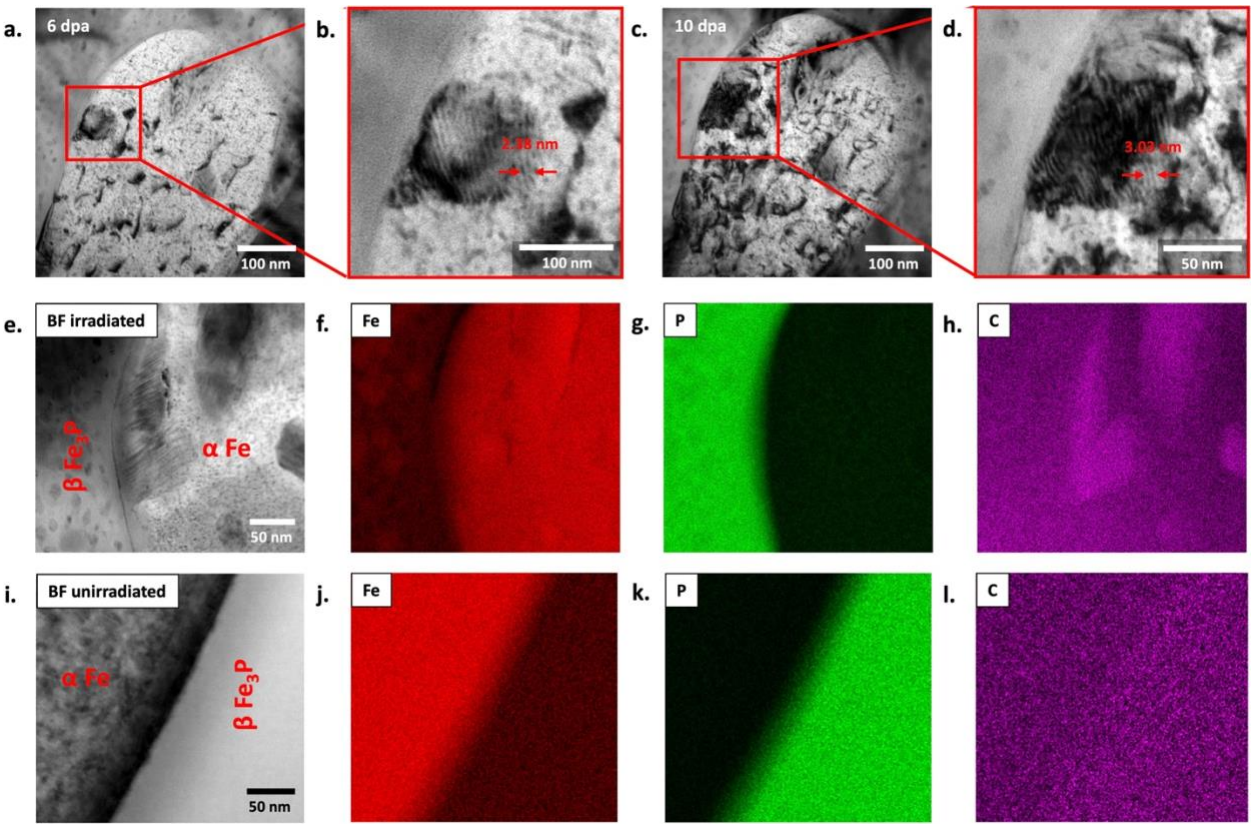

***Figure 7**: Precipitates in α-Fe during in situ irradiation at (a) 6 dpa with (b) corresponding fringe separation measurement, and at (c) 10 dpa with (d) corresponding fringe separation measurement; EDS chemical map of α-Fe irradiated, showing (e) STEM image and corresponding elemental maps of (f) Fe, (g) P, and (h) C; EDS chemical map of unirradiated α-Fe showing (i) STEM image and corresponding elemental maps of (j) Fe, (k) P, and (i) C, Reference image scale bars are representative of all EDS Maps*

By contrast, *in situ* irradiation-induced defect evolution in the Fe-P exhibits a high number density of nanocluster-type defects, without distinct dislocation loop formation as is observed in α-Fe. This observation is consistent with the cluster-type defects observed in Fe-P after *ex situ* irradiation. Bright field TEM micrographs of the tracked region during *in situ* irradiation are shown at doses of 1, 3, 6, and 10 dpa in Figure 8(a)-(b) and (e)-(f). The micrographs reveal nanoclusters nucleate even before 1 dpa, that increase in size with

increasing dose; representative clusters are shown at higher magnification in Figure 8(c)-(d) and (g)-(h). Quantitatively, the cluster density decreases from 1.27 x 10^{23} at 1 dpa to 1.08 x 10^{23} at 10 dpa, while the average cluster size grows from 3.46 ± 1.1 nm at 1 dpa to 5.14 ± 1.6 nm at 10 dpa. The nanocluster number density in the Fe-P is more than one order of magnitude higher than the dislocation loop density in the α-Fe; this is consistent with the significantly denser defect density in Fe-P compared to Fe-Cr and Fe-N following *ex situ* irradiation (Figure 4).

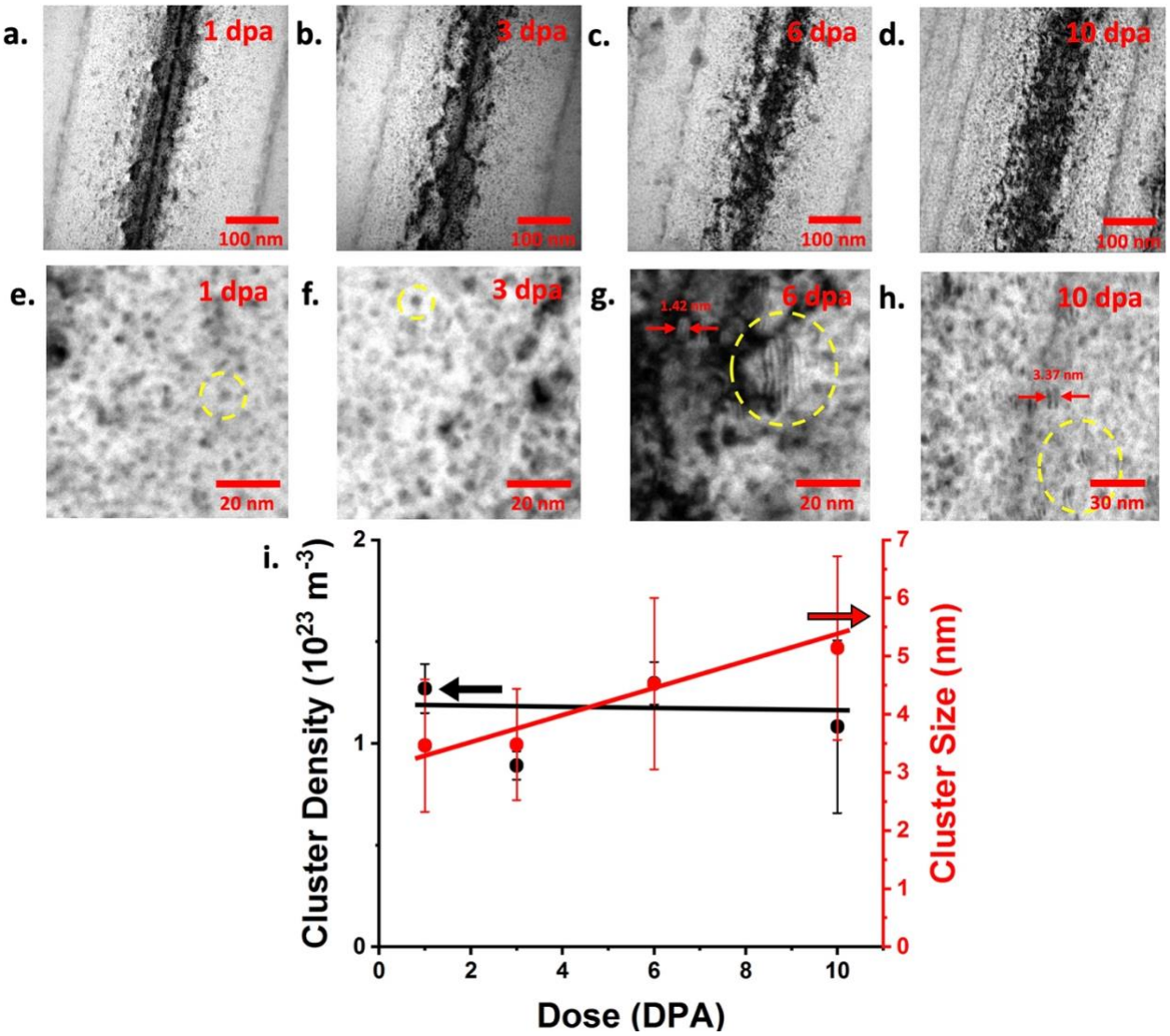

***Figure 8**: Nanocluster and precipitate evolution in Fe-P during in situ irradiation, shown by (a-d) TEM bright field micrographs at doses of 1, 3, 6, and 10 dpa; Enlarged images showing representative clusters and precipitates in (e-f); (i) Plot of nanocluster size and number density as a function of dose.*

The nanoclusters are rich in P and depleted in Fe, as shown in the EDS maps in Figure 9(a)-(e). These chemical analyses confirm the cluster-type nature of these irradiation-induced defects (as opposed to dislocation loop-type defects). Line scans reveal the clusters contain ~9.0 at% P and ~91.0 at% Fe, representing a ~4.5 at% P enrichment and Fe depletion compared to the Fe-P matrix, Figure 9(f)-(g).

Radiation-assisted precipitates ranging in size from 13 to 75 nm also emerge at 6 dpa and are initially identifiable through their corresponding Moiré fringes [26,33], yellow dashed circles in Figure 8(g-h). EDS maps reveal these precipitates are carbides, consistent with the radiation-assisted carbides observed with similar morphologies in the α-Fe. The Moiré fringe separation distributions, Figure 9(m) shift to the right between 6 and 10 dpa. This increase in fringe spacing occurs as the precipitate begins to take on the carbide crystal structure, which exhibits increasing lattice mismatch to the α-Fe [26,33]. Additionally, the standard deviation of the fringe spacing distribution also increases from 6 to 10 dpa, which indicates that new coherent precipitates are continuing to form at 10 dpa, while previously nucleated precipitates are progressing toward complete distinction from the parent α-Fe phase. This progress toward complete phase separation is supported by the emergence of new rings in the diffraction patterns taken at 10 dpa [26], shown in Figure S9 in the supplementary information document.

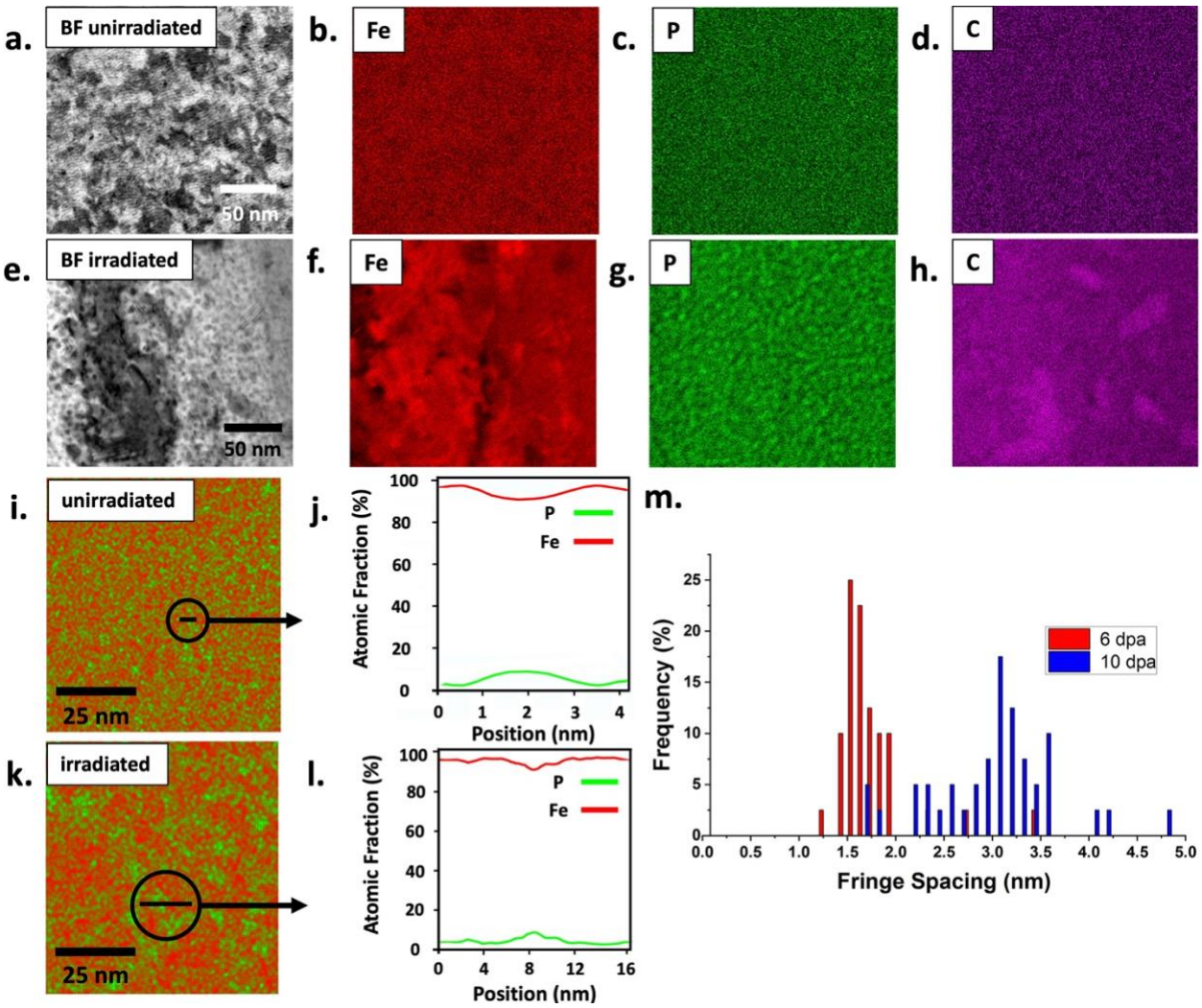

***Figure 9**: EDS chemical map of Fe-P after in situ irradiation, showing (a) STEM image and corresponding elemental maps of (b) Fe, (c) P, and (d) C (scale bar in reference image representative of all EDS maps b-d); Line scans over nanoclusters in EDS maps in (i) unirradiated Fe-P with (j) corresponding Fe and P composition vs position plot and (k) irradiated Fe-P with (l) corresponding Fe and P composition vs position plot; (i) Moiré fringe spacing distribution evolution with increasing dose.*

4. Discussion

The atomic radius misfit between solute and host atoms has long been used as a "rule of thumb" predictor of the extent of irradiation-induced phenomena, such as radiation induced segregation [37,41] and irradiation-induced defect densities. The atomic size factor quantifies the solute misfit by representing the percent difference between the solute and host atom sizes. Details of the calculation of substitutional and interstitial size factor are provided in the supplementary information. For example, Fukuya, et al. find that loop density increases with increasing P (an undersized substitutional atom) content in austenitic Fe-18Cr-9Ni-1.5Mn alloys [42]. Watanabe, et al. [43] demonstrates enhanced defect nucleation and increasing defect density in an austenitic FeCrNi steel with the addition of P. Additionally, Satoh, et al. [44] corroborates the increase in defect density with increasing size factor magnitude in model Cu binary alloys containing undersized substitutional Co, Ni, and Be with size factors of -3.78, -8.46, and -26.45 respectively, attributed to self-interstitial atom (SIA) trapping [37].

The influence of SIA trapping on microstructure evolution and defect densities in irradiated Fe-based alloys is relatively well-understood, particularly for undersized substitutional solutes. Trapping capability is a function of solute-SIA bonding as well as elastic strain resulting from solute/lattice misfit, both factors which negatively impact SIA migration energy [44]. The dislocation loop density is related to SIA mobility in irradiated metals at intermediate temperatures through:

$$C_L = \beta \left(\frac{P}{M_i}\right)^{\frac{1}{2}} \quad (1)$$

where C_L is the loop concentration, β is a constant, P is the production rate of point defects, and M_i is the SIA mobility. The SIA mobility can be further related to SIA migration energy and solute-SIA binding energy through:

$$M_i = \nu e^{\frac{-(E_m+B)}{kT}} \quad (2)$$

where ν is lattice vibrational frequency, E_m is the SIA migration energy, B is the SIA-solute binding energy, k is the Boltzmann constant, and T is the temperature.

These equations show that when the trapping capability is high, few interstitial-solute complexes will dissociate, and defect concentration (i.e., number density) will increase. Furthermore, when production rate of point defects increases, the defect density also increases. Since di-interstitial dumbbells are known dislocation loop nucleation sites and SIA dumbbells tend to be oriented along the <110> direction, these configurations are expected to serve as the predominant configurations for dislocation loop and cluster nucleation sites [45,46]. Furthermore this is the most stable SIA configuration in α-Fe [47].

A density functional theory (DFT) study by Becquart, et al. [48] demonstrates that SIA-solute bond strength increases with increasing size factor magnitude for undersized substitutional solutes. This implies that undersized substitutional solutes with larger size factor magnitudes may have stronger defect trapping, and thus a higher SIA migration energy, possibly resulting in a higher defect density. The Becquart, et al. [48] study also states that smaller atoms are more likely to bond with SIAs in compressional configurations such as <110> dumbbells, potentially stabilizing a high number density of defect nucleation sites. The <110> mixed di-interstitial dumbbell in Fe-P has a binding energy between 1.02 and 1.05 eV as demonstrated by an *ab initio* study by Meslin, et al. [49].

Binding is less strong – and is sometimes negative – for substitutional solutes that have low size factor mismatch or are oversized in Fe. This is particularly demonstrated for compressional defect configurations such as the <110> dumbbell, and thus stable defect

nucleation sites are not likely to be favored [48]. For example, Si, Mn, Ni, and Cu have self-interstitial mixed dumbbell binding energies of 0.01, 0.37, -0.36, and -0.46 eV in Fe [50]. By contrast, interstitial solutes C and N have comparatively weak self-interstitial dumbbell binding energies of -0.19 and -0.58 eV, respectively [27].

Thus, size factor alone does not fully predict defect production; rather, the substitutional or interstitial nature of solutes should also be considered. This idea is supported by the lack of relationship between size factor and defect density for the three alloys in the current study, Figure 4(a). In the remainder of this Discussion section, each of the three alloys will be considered with respect to both size factor and defect density, then placed in the context of the archival literature to draw generalizations.

4.1 Substitutional and Undersized Solute: P

The role of P on irradiation-induced defect morphologies has been well established in the literature. In one study, Pareige, et al. demonstrated that P addition stabilizes defect clusters in a ferritic-martensitic Fe9at%Cr and Fe12at%Cr alloys under ion irradiation [45]. Meanwhile, Watanabe, et al. observed P additions to enhance loop nucleation and increase loop density in a FeCrNi [43], due to the high binding energy between P atoms and interstitials. Likewise, the current results which show a high number density and small size of defects in Fe-P are also attributed to strong self-interstitial atom (SIA) trapping by significantly undersized substitutional P atoms, which have a size factor of -13.6% in bcc Fe [31]. In general, undersized atoms tend to enhance the stability of SIA mixed interstitial dumbbells and consequently enhance defect formation [44,51,52]. Indeed, *ab initio* calculations for Fe-P predict several

stable <110> di-interstitial mixed Fe-P dumbbell configurations, resulting in higher SIA migration energies, limited dissociation of defect nucleation sites, and thus a high concentration of defects [28,53]. At these defect sites, undersized P atoms tend to enrich and form clusters [37,44], leading to stabilization and limited growth of these clusters [53]. Furthermore, upon being trapped, solute atoms with a large size factor magnitude, such as P in Fe, segregate to the defect core and reduce its sink strength for absorption of SIAs, limiting the growth of these defects [44]. Additionally, strong P-vacancy binding can result in vacancy drag effects, which further increase migration energy, thus limiting defect growth [28,54,55].

An additional effect of P as a substitutional solute is to retard the irradiation-assisted nucleation of carbides, which initially appear at a lower damage level (3 dpa) in α-Fe than in Fe-P (6 dpa). Both P, an undersized substitutional atom, and C, an interstitial atom, are expected to diffuse via the interstitial flux. In the α-Fe region where there is negligible P, interstitial C does not face competition to diffuse via interstitial flux. But on the other hand, in the Fe-P region where P composition is relatively high, both C and P diffuse via the interstitial flux, and will compete for segregation sites. This competition slows, though does not eliminate, carbide formation in the Fe-P region. Similarly, P has been shown to inhibit MC-type carbide formation in a Ni-Fe superalloy in work by Sun, et al. [12].

The role of P in stabilizing defects is most distinct when comparing the *in situ* defect evolution in the α-Fe to that in the Fe-P. While the α-Fe exhibits clear development of easily resolvable dislocation loops, essentially no dislocation loops are resolvable in the Fe-P. In the Fe-P, since P atoms trap SIAs, limit defect growth, and tend to enrich defect sites, defect clusters grow into P-rich nanoprecipitates rather than developing into dislocation loops.

Conversely, in the low-P α-Fe region, SIAs can migrate more freely and contribute to dislocation loop formation and growth. Moreover, these dislocation loops will not get pinned by P atoms and can thus glide toward other loops or the lamella surface [8,36].

4.2 Substitutional and Oversized Solute: Cr

Since the Cr atom is slightly oversized in α-Fe with a size factor of +4.36, there is less space available in the lattice, and it is more difficult for di-interstitials to form, so these dislocation loop nucleation sites will be less prevalent than in the Fe-P system. When Cr di-interstitials are able to form, they tend to arrange as <111> crowdions which can also act as dislocation loop nucleation sites, but they are less stable than <110> dumbbells [37,47,56]. The <111> crowdion configuration consists of an SIA compressed in between a corner atom and the center atom along a <111> direction. Atoms along the <111> direction shift to accommodate the extra atom, such that 7 to 10 atoms share 6 to 9 atomic positions, spreading the strain over those atomic positions and accommodating the oversized solute atom [37]. Works from Terentyev and Becquart, et al. show the stronger binding energy of Cr to the <111> crowdion than to other defect configurations such as the <110> dumbbell [48,56]. Terentyev [56] also demonstrates that <111> crowdions tend to form larger cluster and dislocation loop defects than do <110> dumbbells. Furthermore, the <111> crowdions can readily migrate by 1D random walk [37], which may facilitate defect agglomeration and coarsening (i.e., larger defect sizes at lower number densities). This explains the larger defect sizes and lower defect number densities in the Fe-Cr than in Fe-P.

4.3 Interstitial and Undersized Solute: N

As an interstitial atom which occupies an octahedral site in α-Fe, N produces a large lattice distortion in the α-Fe lattice and has a size factor of +70.5 [30]. Similar to oversized Cr in α-Fe, N will occupy more space in the α-Fe lattice and less volume will be available for di-interstitial defects to form, resulting in fewer dislocation loop nucleation sites. Hence, a depressed defect density will result in the irradiated Fe-N alloy, but defects will be able to grow to larger sizes. This is consistent with a study by Rice, et al., which shows that the addition of N to model ferritic Fe-based binary and ternary alloys enables dislocation loops to grow to larger diameters [57]. Another study from Aydogan, et al. also concurs that increasing N content tends to reduce dislocation loop density and increase dislocation loop sizes in 12Cr F/M alloy HT9, attributed to N-SIA coupling that stabilizes dislocation loops [18]. Similarly, the present study finds the largest defect diameters and lower defect densities in the Fe-N specimen.

4.4 Influence of Solute Concentration on Defect Densities

Certainly, the three Fe binary alloys exhibit disparate defect densities and the question of the influence of the solute concentration must be answered. The Fe-9.5Cr alloy has the highest solute concentration followed by the Fe-4.5P alloy and the Fe-N2.3N alloy has the lowest of the solute concentrations. With respect to Cr in Fe there have been mixed results regarding the influence of solute concentration on the density of dislocation loops or interstitial/vacancy clusters. W. Chen et al, for instance, demonstrated an increase in defect density with increased Cr composition in a ferritic/martensitic Fe-Cr alloy with increasing Cr concentration from 0 to 16at% [58] while a study by S.I. Porollo et al. showed no correlation [59]. If the former is correct, a reduction in the concentration of Cr in the Fe-Cr binary alloy may

suppress the defect density further. A study by Aydogan et al. demonstrated a reduction of the defect density with the increase in N content in ion irradiated HT9 alloys with high and low N content. The high N HT9 alloy exhibited a lower defect density than the low N HT9 alloy. This study supports the analysis that N suppresses irradiated defect densities from section 4.3, and an increase in the composition of N may result in further suppression. The composition of P may also play a role in the enhancement or suppression of irradiation defect densities. A study by Watanabe et al. demonstrated an increase in defect density with increasing P content in an austenitic Fe-Cr-Ni alloy [43]. A study by Y. Chen et al demonstrated that the composition of undersized Si in an ion irradiated 9Cr ferritic / martensitic steel had some positive influence on dislocation loop density. However, the loop density only increased by ~38% with a %150 increase in Si concentration [60]. As such, the difference in solute composition is not expected to invalidate the underlying trend posited in this study.

4.5 Comparison to Other Binary Alloys

Results from the current study are compiled with data from the archival literature [44,61–68] to compare irradiation-induced defect densities as a function of atomic size factor across a variety of binary alloys, Figure 10. (A comprehensive list of the literature data used in this figure is provided in Table S1 in the supplementary information.) This literature survey is limited only to binary alloys, which enable isolation of the effects of individual solutes. Data available in the literature is limited and non-systematic, all being done on different binary alloys and using inconsistent experimental conditions such as different irradiation doses, dose rates, temperatures, solute concentrations, and irradiating particle types. Nevertheless, some general trends can be discerned that support the projections of DFT and *ab initio* models.

Figure 10 categorizes data by solute type – interstitial, oversized substitutional, and undersized substitutional. The figure reveals a loosely positive correlation between defect density and size factor for undersized substitutional solutes. This suggests that the smaller the substitutional atom, the stronger its tensile elastic strain field, resulting in greater ease of di-interstitial dumbbell formation, and thus strengthening its effectiveness as a SIA trap. This is consistent with Becquart's [48] DFT calculation that SIA-solute bond strength increases with size factor for undersized substitutional solutes.

On the other hand, oversized substitutional solutes with large size factor magnitude appear to be correlated with a depressed defect density. This is likely because SIA-solute binding for oversized substitutional solutes is relatively unstable in the conventional <110> dumbbell configuration, resulting in these oversized solutes tending to take on alternative configurations [48]. Consequently, clusters and dislocation loops have limited opportunity to nucleate and grow around oversized substitutional solutes. Meanwhile, oversized substitutional solutes with smaller size factor magnitudes exhibit a wide spread of defect densities, which may support a trapping mechanism based on chemical attraction instead of purely elastic interactions [48].

Lastly, interstitials also seem to depress defect nucleation similarly to oversized solutes with large size factors. This is because the nature of an interstitial atom is to occupy the space that is needed to form SIA di-interstitial defects, which act as cluster and dislocation loop nucleation sites. Furthermore, since interstitials tend to be unstable in shared sites such as the <110> dumbbell or <111> crowdion positions [27], interstitials may instead migrate back to a

single interstitial site. The compressive elastic strain of these interstitials limits their strength as defect nucleation sites.

Defect densities of the Fe-Cr, Fe-N, and Fe-P alloys in the current study are consistent with the trends identified in Figure 10, which fall into agreement atomistic simulations. However, it is worth reemphasizing that only limited data are available on binary alloys, and these data encompass a wide variety of materials and experimental conditions. More systematic studies are necessary for definitive trends to be extracted. Nevertheless, Figure 10 reveals that both size factor and the position (i.e., substitutional or interstitial) of solutes must be considered when utilizing compositional tailoring to engineer tolerance to irradiation defect formation.

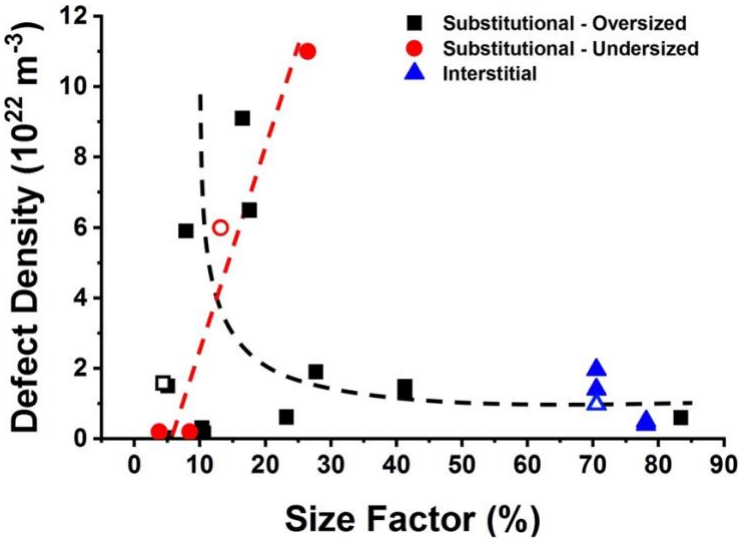

***Figure 10**: Irradiation-induced defect density as a function of size factor (%) for undersized substitutional solutes (red), oversized substitutional solutes (black), and interstitial solutes (blue); open symbols represent data from the current study.*

5. Conclusions

Three Fe-based binary alloys are selected to investigate the effect of solute size and solute position (i.e., substitutional or interstitial), on the development of irradiation-induced defects. The alloys selected for study are Fe-9.5%Cr (Cr as oversized substitutional solute), Fe-4.5%P (P as undersized substitutional solute), and Fe-2.3%N (N as undersized interstitial solute). The three alloys are irradiated *ex situ* with 4.4 MeV Fe^{2+} ions to 8.5 dpa. The Fe-P alloy, comprised of a dual-phase structure of Fe-4.5%P and pure α-Fe regions, is also irradiated *in situ* in a TEM with 1 MeV Kr^{2+} ions at 370°C up to 10 dpa. Post-irradiation TEM characterization enables the following key conclusions to be drawn:

- The Fe-P exhibits a considerably finer and denser population of irradiation-induced defects than the Fe-Cr and Fe-N.
- In Fe-P compared to pure α-Fe, strong defect trapping at P solutes produces a high density of P-rich clusters while limiting dislocation loop nucleation and growth. The presence of P also slows radiation-assisted carbide formation.
- Alloying with undersized substitutional solutes (e.g., P) may stabilize a high density of strong defect trapping sites, thus generating a dense population of defect nanoclusters with limited ability to develop extended defects such as dislocation loops.
- Alloying with oversized substitutional solutes (e.g., Cr) and interstitials (e.g., N) may suppress the development of extended defects such as dislocation loops because of weak solute-defect trapping owing to the compressive stresses of these solutes.

Acknowledgements

The authors thank Dr. Ovidiu Toader, formerly of the Michigan Ion Beam Laboratory (MIBL) for assistance with *ex situ* ion irradiation, and Dr. Matthew Besser at Ames Laboratory for assistance with alloy fabrication. This research was sponsored by the National Science Foundation award DMR-17-52636. The TEM in situ irradiation at the IVEM-Tandem Facility at Argonne National Laboratory was supported by the US DOE Office of Nuclear Energy through a Nuclear Science User Facilities (NSUF) rapid turnaround experiment.

References

[1] C. Cabet, F. Dalle, E. Gaganidze, J. Henry, H. Tanigawa, Ferritic-martensitic steels for fission and fusion applications, Journal of Nuclear Materials. 523 (2019) 510–537. https://doi.org/10.1016/J.JNUCMAT.2019.05.058.

[2] E. Wakai, N. Okubo, M. Ando, T. Yamamoto, F. Takada, Reduction method of DBTT shift due to irradiation for reduced-activation ferritic/martensitic steels, Journal of Nuclear Materials. 398 (2010) 64–67. https://doi.org/10.1016/J.JNUCMAT.2009.10.011.

[3] H. Kayano, A. Kimura, M. Narui, Y. Sasaki, Y. Suzuki, S. Ohta, Irradiation embrittlement of neutron-irradiated low activation ferritic steels, Journal of Nuclear Materials. 155–157 (1988) 978–981. https://doi.org/10.1016/0022-3115(88)90452-7.

[4] Irradiation responses and defect behavior of single-phase concentrated solid solution alloys, United States. Dept. of Energy. Office of Science, Washington, D.C, 2018.

[5] W.Y. Chen, Y. Miao, J. Gan, M.A. Okuniewski, S.A. Maloy, J.F. Stubbins, Neutron irradiation effects in Fe and Fe-Cr at 300 °c, Acta Mater. 111 (2016). https://doi.org/10.1016/j.actamat.2016.03.060.

[6] S.J. Zinkle, G.S. Was, Materials challenges in nuclear energy, Acta Mater. 61 (2013). https://doi.org/10.1016/j.actamat.2012.11.004.

[7] P.D. Edmondson, S.A. Briggs, Y. Yamamoto, R.H. Howard, K. Sridharan, K.A. Terrani, K.G. Field, Irradiation-enhanced α' precipitation in model FeCrAl alloys, Scr Mater. 116 (2016). https://doi.org/10.1016/j.scriptamat.2016.02.002.

[8] M.L. Jenkins, Z. Yao, M. Hernández-Mayoral, M.A. Kirk, Dynamic observations of heavy-ion damage in Fe and Fe-Cr alloys, Journal of Nuclear Materials. 389 (2009). https://doi.org/10.1016/j.jnucmat.2009.02.003.

[9] Z. Yao, M. Hernandez-Mayoral, M.L. Jenkins, M.A. Kirk, Heavy-ion irradiations of Fe and Fe-Cr model alloys Part 1: Damage evolution in thin-foils at lower doses, Philosophical Magazine. 88 (2008). https://doi.org/10.1080/14786430802380469.

[10] S. Xu, Z. Yao, M.L. Jenkins, TEM characterisation of heavy-ion irradiation damage in FeCr alloys, Journal of Nuclear Materials. 386–388 (2009). https://doi.org/10.1016/j.jnucmat.2008.12.078.

[11] Y. Pachaury, T. Kumagai, J.P. Wharry, A. El-Azab, A data science approach for analysis and reconstruction of spinodal-like composition fields in irradiated FeCrAl alloys, Acta Mater. 234 (2022) 118019. https://doi.org/10.1016/J.ACTAMAT.2022.118019.

[12] W.R. Sun, S.R. Guo, D.Z. Lu, Z.Q. Hu, Effect of phosphorus on the microstructure and stress rupture properties in an Fe-Ni-Cr base superalloy, Metall Mater Trans A Phys Metall Mater Sci. 28 (1997) 649–654. https://doi.org/10.1007/s11661-997-0050-5.

[13] C. Wang, H. Zhao, Y. Guo, J. Guo, L. Zhou, Structural stability and mechanical properties of phosphorus modified Ni-Fe based superalloy GH984, in: Materials Research Innovations, 2014. https://doi.org/10.1179/1432891714Z.000000000833.

[14] S.K. Ray, S. Mishra, O.N. Mohanty, Magnetic aging characteristics of a phosphorous-bearing low carbon steel, Scripta Metallurgica. 15 (1981) 971–973. https://doi.org/10.1016/0036-9748(81)90236-2.

[15] S.K. Ray, S. Mishra, O.N. Mohanty, TEM study of carbide precipitation in a phosphorus-bearing low-carbon steel, Scripta Metallurgica. 16 (1982) 43–47. https://doi.org/10.1016/0036-9748(82)90400-8.
[16] H. Watanabe, A. Aoki, H. Murakami, T. Muroga, N. Yoshida, Effects of phosphorus on defect behavior, solute segregation and void swelling in electron irradiated FeCrNi alloys, Journal of Nuclear Materials. 155–157 (1988). https://doi.org/10.1016/0022-3115(88)90422-9.
[17] C.J. Rietema, M.R. Chancey, S.K. Ullrich, C.B. Finfrock, D.V. Marshall, B.P. Eftink, Y.Q. Wang, G.R. Bourne, S.A. Maloy, A.J. Clarke, K.D. Clarke, The influence of nitrogen and nitrides on the structure and properties of proton irradiated ferritic/martensitic steel, Journal of Nuclear Materials. 561 (2022). https://doi.org/10.1016/j.jnucmat.2022.153528.
[18] E. Aydogan, J. Gigax, S. Parker, B.P. Eftink, M. Chancey, J.D. Poplawsky, S. Maloy, Nitrogen effects on radiation response in 12Cr ferritic/martensitic alloys, Scr Mater. 189 (2020).
[19] C.J. Rietema, M.R. Chancey, S.K. Ullrich, C.B. Finfrock, D.V. Marshall, B.P. Eftink, Y.Q. Wang, G.R. Bourne, S.A. Maloy, A.J. Clarke, K.D. Clarke, The influence of nitrogen and nitrides on the structure and properties of proton irradiated ferritic/martensitic steel, Journal of Nuclear Materials. 561 (2022). https://doi.org/10.1016/j.jnucmat.2022.153528.
[20] H. Kim, J.G. Gigax, C.J. Rietema, O. el Atwani, M.R. Chancey, J.K. Baldwin, Y. Wang, S.A. Maloy, Void swelling of conventional and composition engineered HT9 alloys after high-dose self-ion irradiation, Journal of Nuclear Materials. 560 (2022) 153492. https://doi.org/10.1016/j.jnucmat.2021.153492.
[21] E.A. Little, D.R. Harries, The Correlation of Radiation-Hardening with Interstitial Nitrogen Content in Mild Steels, Metal Science Journal. 4 (1970) 195–200. https://doi.org/10.1179/msc.1970.4.1.195.
[22] E.A. Little, D.R. Harries, Radiation-Hardening and Recovery in Mild Steels and the Effects of Interstitial Nitrogen, Metal Science Journal. 4 (1970) 188–195. https://doi.org/10.1179/msc.1970.4.1.188.
[23] O.K. von Goldbeck, IRON—Binary Phase Diagrams, 1982. https://doi.org/10.1007/978-3-662-08024-5.
[24] K.H. Yano, M.J. Swenson, Y. Wu, J.P. Wharry, TEM in situ micropillar compression tests of ion irradiated oxide dispersion strengthened alloy, Journal of Nuclear Materials. 483 (2017) 107–120. https://doi.org/10.1016/j.jnucmat.2016.10.049.
[25] Application of STEM characterization for investigating radiation effects in BCC Fe-based alloys, United States. Dept. of Energy. Office of Science, Washington, D.C, 2015.
[26] David. Brandon, Microstructural Characterization of Materials, 2nd ed., Wiley, Hoboken, 2008.
[27] C. Domain, Ab initio study of foreign interstitial atom (C, N) interactions with intrinsic point defects in alpha-Fe, Phys Rev B Condens Matter Mater Phys. 69 (2004) 144112. https://doi.org/info:doi/.
[28] C. Domain, C.S. Becquart, Diffusion of phosphorus in α-Fe: An ab initio study, Phys Rev B Condens Matter Mater Phys. 71 (2005). https://doi.org/10.1103/PhysRevB.71.214109.

[29] J.-H. Shim, H.-J. Lee, B.D. Wirth, Molecular dynamics simulation of primary irradiation defect formation in Fe–10%Cr alloy, Journal of Nuclear Materials. 351 (2006) 56–64. https://doi.org/10.1016/j.jnucmat.2006.02.021.
[30] H.W. King, Quantitative size-factors for interstitial solid solutions, J Mater Sci. 6 (1971). https://doi.org/10.1007/BF00550085.
[31] H.W. King, Quantitative size-factors for metallic solid solutions, J Mater Sci. 1 (1966). https://doi.org/10.1007/BF00549722.
[32] M.J. Swenson, J.P. Wharry, TEM characterization of irradiated microstructure of Fe-9%Cr ODS and ferritic-martensitic alloys, Journal of Nuclear Materials. 502 (2018) 30–41. https://doi.org/10.1016/J.JNUCMAT.2018.01.062.
[33] H.S. Nalwa, Handbook of surfaces and interfaces of materials, Academic Press, San Diego, 2001.
[34] Q. Yuan, A. Chauhan, E. Gaganidze, J. Aktaa, In-situ TEM investigations of dislocation loop annealing kinetics in neutron-irradiated 9%Cr RAFM steel, Journal of Nuclear Materials. 558 (2022) 153365. https://doi.org/10.1016/j.jnucmat.2021.153365.
[35] R. Schaublin, B. Decamps, A. Prokhodtseva, J.F. Loffler, On the origin of the primary 1/2 a.sub.0 and a.sub.0 loops in irradiated Fe alloys, Acta Mater. 133 (2017) 427. https://doi.org/10.1016/j.actamat.2017.02.041.
[36] J.C. Haley, S.A. Briggs, P.D. Edmondson, K. Sridharan, S.G. Roberts, S. Lozano-Perez, K.G. Field, Dislocation loop evolution during in-situ ion irradiation of model FeCrAl alloys, Acta Mater. 136 (2017). https://doi.org/10.1016/j.actamat.2017.07.011.
[37] G.S. Was, Fundamentals of radiation materials science: Metals and alloys, second edition, 2016. https://doi.org/10.1007/978-1-4939-3438-6.
[38] H. Kim, J.G. Gigax, O. El-Atwani, M.R. Chancey, J.K. Baldwin, Y. Wang, S.A. Maloy, Comparison of void swelling of ferritic-martensitic and ferritic HT9 alloys after high-dose self-ion irradiation, Mater Charact. 173 (2021) 110908. https://doi.org/10.1016/J.MATCHAR.2021.110908.
[39] J.G. Gigax, H. Kim, E. Aydogan, F.A. Garner, S. Maloy, L. Shao, Beam-contamination-induced compositional alteration and its neutron-atypical consequences in ion simulation of neutron-induced void swelling, Mater Res Lett. 5 (2017). https://doi.org/10.1080/21663831.2017.1323808.
[40] N.T.H. Farr, G.M. Hughes, C. Rodenburg, Monitoring carbon in electron and ion beam deposition within fib-sem, Materials. 14 (2021). https://doi.org/10.3390/ma14113034.
[41] G.S. Was, J.P. Wharry, B. Frisbie, B.D. Wirth, D. Morgan, J.D. Tucker, T.R. Allen, Assessment of radiation-induced segregation mechanisms in austenitic and ferritic–martensitic alloys, Journal of Nuclear Materials. 411 (2011) 41–50. https://doi.org/10.1016/j.jnucmat.2011.01.031.
[42] K. Fukuya, S. Nakahigashi, S. Ozaki, S. Shima, Effects of phosphorus, silicon and sulphur on microstructural evolution in austenitic stainless steels during electron irradiation, Journal of Nuclear Materials. 179 (1991) 1057–1060. https://doi.org/10.1016/0022-3115(91)90274-B.
[43] H. Watanabe, A. Aoki, H. Murakami, T. Muroga, N. Yoshida, Effects of phosphorus on defect behavior, solute segregation and void swelling in electron irradiated Fe-Cr-Ni

alloys, Journal of Nuclear Materials. 155–157 (1988) 815–822. https://doi.org/10.1016/0022-3115(88)90422-9.
[44] Y. Satoh, T. Yoshiie, S. Arai, Undersize solute element effects on defect structure development in copper under electron irradiation, Philosophical Magazine. 98 (2018). https://doi.org/10.1080/14786435.2017.1414326.
[45] C. Pareige, V. Kuksenko, P. Pareige, Behaviour of P, Si, Ni impurities and Cr in self ion irradiated Fe–Cr alloys – Comparison to neutron irradiation, Journal of Nuclear Materials. 456 (2015) 471–476. https://doi.org/10.1016/j.jnucmat.2014.10.024.
[46] E. Meslin, C.-C. Fu, A. Barbu, F. Gao, F. Willaime, Theoretical study of atomic transport via interstitials in dilute Fe − P alloys, Phys Rev B Condens Matter Mater Phys. 75 (2007). https://doi.org/10.1103/PhysRevB.75.094303.
[47] C. Domain, C.S. Becquart, Ab initio calculations of defects in Fe and dilute Fe-Cu alloys, Phys Rev B Condens Matter. 65 (2001). https://doi.org/10.1103/PhysRevB.65.024103.
[48] C.S. Becquart, R. Ngayam Happy, P. Olsson, C. Domain, A DFT study of the stability of SIAs and small SIA clusters in the vicinity of solute atoms in Fe, Journal of Nuclear Materials. 500 (2018) 92–109. https://doi.org/10.1016/J.JNUCMAT.2017.12.022.
[49] E. Meslin, C.C. Fu, A. Barbu, F. Gao, F. Willaime, Theoretical study of atomic transport via interstitials in dilute Fe-P alloys, Phys Rev B Condens Matter Mater Phys. 75 (2007). https://doi.org/10.1103/PhysRevB.75.094303.
[50] E. Vincent, C.S. Becquart, C. Domain, Ab initio calculations of self-interstitial interaction and migration with solute atoms in bcc Fe, Journal of Nuclear Materials. 359 (2006). https://doi.org/10.1016/j.jnucmat.2006.08.022.
[51] A. Bakaev, D. Terentyev, G. Bonny, T.P.C. Klaver, P. Olsson, D. van Neck, Interaction of minor alloying elements of high-Cr ferritic steels with lattice defects: An ab initio study, Journal of Nuclear Materials. 444 (2014) 237–246. https://doi.org/10.1016/j.jnucmat.2013.09.053.
[52] T. Hayashi, K. Fukumoto, H. Matsui, Effect of undersized solute atoms on point defect behavior in V-A (A = Fe, Cr and Si) binary alloys studied by using HVEM, Journal of Nuclear Materials. 307–311 (2002). https://doi.org/10.1016/S0022-3115(02)01162-5.
[53] C. Pareige, V. Kuksenko, P. Pareige, Behaviour of P, Si, Ni impurities and Cr in self ion irradiated Fe-Cr alloys - Comparison to neutron irradiation, Journal of Nuclear Materials. 456 (2015). https://doi.org/10.1016/j.jnucmat.2014.10.024.
[54] A.A. Vasiliev, V. v. Rybin, A.A. Zisman, The nature of the phosphorus atom mobility in bcc iron irradiated at low temperatures, Journal of Nuclear Materials. 231 (1996). https://doi.org/10.1016/0022-3115(96)00201-2.
[55] L. Messina, T. Schuler, M. Nastar, M.-C. Marinica, P. Olsson, Solute diffusion by self-interstitial defects and radiation-induced segregation in ferritic Fe–X (X=Cr, Cu, Mn, Ni, P, Si) dilute alloys, Acta Mater. 191 (2020) 166–185. https://doi.org/10.1016/j.actamat.2020.03.038.
[56] D. Terentyev, Study of radiation effects in FeCr alloys for fusion applications using computer simulations, Phd Thesis. (2006).
[57] P.M. Rice, R.E. Stoller, The effect of solutes on defect distributions and hardening in ion-irradiated model ferritic alloys, Journal of Nuclear Materials. 244 (1997). https://doi.org/10.1016/s0022-3115(96)00753-2.

[58] W.Y. Chen, Y. Miao, J. Gan, M.A. Okuniewski, S.A. Maloy, J.F. Stubbins, Neutron irradiation effects in Fe and Fe-Cr at 300 °C, Acta Mater. 111 (2016) 407–416. https://doi.org/10.1016/J.ACTAMAT.2016.03.060.
[59] S.I. Porollo, A.M. Dvoriashin, A.N. Vorobyev, Y. v. Konobeev, The microstructure and tensile properties of Fe–Cr alloys after neutron irradiation at 400°C to 5.5–7.1 dpa, Journal of Nuclear Materials. 256 (1998) 247–253. https://doi.org/10.1016/S0022-3115(98)00043-9.
[60] Y. Chen, Y. Long, H. Luo, Z. Xie, W. Lin, L. Guo, H. Wang, X. An, Q. Kong, W.P. Zhang, Y. Gao, Y. Wen, Effects of different silicon content on irradiation defects and hardening in 9Cr ferritic/martensitic steel, Journal of Nuclear Materials. 571 (2022) 154026. https://doi.org/10.1016/J.JNUCMAT.2022.154026.
[61] Y. Satoh, T. Yoshiie, I. Ishida, M. Kiritani, Defect structure development in electron-irradiated Cu-based Si, Ge and Sn binary alloys, Philosophical Magazine A: Physics of Condensed Matter, Structure, Defects and Mechanical Properties. 80 (2000). https://doi.org/10.1080/01418610008216493.
[62] T. ni Yang, C. Lu, G. Velisa, K. Jin, P. Xiu, M.L. Crespillo, Y. Zhang, H. Bei, L. Wang, Effect of alloying elements on defect evolution in Ni-20X binary alloys, Acta Mater. 151 (2018) 159–168. https://doi.org/10.1016/J.ACTAMAT.2018.03.054.
[63] P. Xiu, Y.N. Osetsky, L. Jiang, G. Velisa, Y. Tong, H. Bei, W.J. Weber, Y. Zhang, L. Wang, Dislocation loop evolution and radiation hardening in nickel-based concentrated solid solution alloys, Journal of Nuclear Materials. 538 (2020). https://doi.org/10.1016/j.jnucmat.2020.152247.
[64] Y. Abe, T. Suzudo, S. Jitsukawa, T. Tsuru, T. Tsukada, Effects of Carbon Impurity on Microstructural Evolution in Irradiated α-Iron, Fusion Science and Technology. 62 (2012) 139–144. https://doi.org/10.13182/FST12-A14126.
[65] V. JANSSON, M. CHIAPETTO, L. MALERBA, The nanostructure evolution in Fe-C systems under irradiation at 560 K, Journal of Nuclear Materials. 442 (2013) 341–349. https://doi.org/10.1016/j.jnucmat.2013.09.017.
[66] H. Watanabe, A. Hiragane, S. Shin, N. Yoshida, Y. Kamada, Effect of stress on radiation-induced hardening of A533B and Fe-Mn model alloys, Journal of Nuclear Materials. 442 (2013). https://doi.org/10.1016/j.jnucmat.2013.04.029.
[67] Y. Satoh, T. Yoshiie, I. Ishida, M. Kiritani, Defect structure development in electron-irradiated Cu-based Si, Ge and Sn binary alloys, Philosophical Magazine. A, Physics of Condensed Matter. Defects and Mechanical Properties. 80 (2000) 2567–2590. https://doi.org/10.1080/01418610008216493.
[68] T. Hamaoka, Y. Satoh, H. Matsui, One-dimensional motion of interstitial clusters in iron-based binary alloys observed using a high-voltage electron microscope, Journal of Nuclear Materials. 433 (2013). https://doi.org/10.1016/j.jnucmat.2012.09.007.